Analytical boundary integral solutions for cracks and thin fluid-filled layers in a 3D poroelastic solid in time and wavenumber domain

Elías R. Heimisson *

Institute of Earth Sciences, University of Iceland, Reykjavík, Iceland
Swiss Seismological Service, ETH Zurich, Zurich, Switzerland

ARTICLE INFO

ABSTRACT

The spectral boundary integral (SBI) method has been widely employed in the study of fractures and friction within elastic and elastodynamic media, given its natural applicability to thin or infinitesimal interfaces. Many such interfaces and layers are also prevalent in porous, fluid-filled media. In this work, we introduce analytical SBI equations for cracks and thin layers in a 3D medium, with a particular focus on fluid presence within these interfaces or layers. We present three distinct solutions, each based on different assumptions: arbitrary pressure boundary conditions, arbitrary flux boundary conditions, or a bi-linear pressure profile within the layer. The bi-linear pressure solution models the flux through a thin, potentially pressurized, leaky layer. We highlight conditions under which the bi-linear SBI equations simplify to either the arbitrary flux or arbitrary pressure SBI equations, contingent on a specific non-dimensional parameter. We then delve into the in-plane pressure effects arising from a shear crack in a poroelastic solid. While such pressurization has been suggested to influence frictional strength in various ways and only occurs in mode II sliding, our findings indicate that a significant portion of the crack face is affected in 3D scenarios. Additionally, we investigate non-dimensional timescales governing the potential migration of this pressurization beyond the crack tip, which could induce strength alterations beyond the initially ruptured area.

1. Introduction

The spectral boundary integral method (SBIM) is a subset of boundary integral methods that employs the superposition of analytical solutions in the time-wavenumber domain (both time and spatial Fourier domains). The term "spectral" denotes expansion using a spectral or Fourier basis. Leveraging the highly efficient Fast Fourier Transform (FFT) algorithms, this method offers an optimal approach for simulating problems like crack propagation and frictional slip on planar interfaces. It has been widely adopted in fields such as engineering, mechanics, and geophysics. However, like other boundary integral methods, SBIM is typically constrained to linear material properties and straightforward geometries. Consequently, its primary applications center around interface friction and fracture in both dynamic and quasi-static elasticity.

The FFT, as previously mentioned in the context of SBIM, has been utilized in boundary integral methods addressing frictional and fracture issues in elastic solids. This allows for efficient spatial convolution (e.g. Quin and Das, 1989; Rice, 1993), while still employing Green's functions or fundamental solutions in the conventional space–time domain. Although SBIM leverages FFT, it

---

* Correspondence to: Institute of Earth Sciences, University of Iceland, Reykjavík, Iceland.
E-mail address: eliasrafn@hi.is.

distinctly employs analytical solutions in both time and wavenumber domains, indicating that one or more spatial dimensions undergo Fourier transformation. In line with other boundary integral methods, SBIM relies on the superposition of analytical solutions. Additionally, it establishes relationships between two interconnected fields, such as slip and shear stress, presenting them as algebraic expressions in the Fourier domain. Illustrative examples of this concept will be provided in subsequent sections.

The derivation and application of spectral boundary integral equations have predominantly been confined to two primary problem classes. The first encompasses quasi-static and fully elastodynamic full-spaces (e.g., Geubelle and Rice, 1995; Perrin and Rice, 1994; Lapusta et al., 2000; Lapusta and Liu, 2009), while the second pertains to quasi-static and fully elastodynamic half-spaces (e.g., Geubelle and Breitenfeld, 1997; Breitenfeld and Geubelle, 1998). A particularly promising advancement in the use of half-space spectral boundary integral solutions is their coupling with volume-based methods in hybrid schemes (Hajarolasvadi and Elbanna, 2017; Ma et al., 2019; Albertini et al., 2021). This strategy facilitates the truncation of extensive computational domains by substituting them with a half-space, represented through a dimensionally reduced boundary integral. Such an approach not only significantly enhances computational efficiency but also offers an economical solution to a prevalent challenge in simulating wave propagation using volume-based methods: the reflections from artificial boundaries.

While the advancements and applications of spectral boundary integral equations have been pivotal in understanding various geophysical and geomechanical phenomena related to friction and fracture, another crucial aspect of geomechanics is the behavior of geo-materials in contact with fluids. Specifically, the study of materials that exhibit both fluid-filled porous structures and elastic properties – known as poroelasticity – has garnered significant attention. This is particularly relevant when considering the intricate interplay between solid and fluid phases in fault structures, which can have profound implications for earthquake and fault mechanics.

With this context in mind, the study of fracture and frictional problems within a poroelastic medium boasts a rich history (e.g., Rudnicki and Koutsibelas, 1991; Atkinson and Craster, 1991; Rudnicki and Rice, 2006). This attention is well-justified, given its profound relevance to earthquake and fault mechanics. Notably, in the shallow crust – where the majority of earthquakes transpire – the crust exhibits behavior akin to a poroelastic solid (Jónsson et al., 2003). In recent times, the poroelastic properties of the crust have been explored in various problems associated with fault slip or the triggering of seismicity during injection/extraction processes (e.g., Segall and Lu, 2015; Chang and Segall, 2016; Rinaldi et al., 2020). Moreover, there is a growing interest in understanding earthquake or frictional ruptures within a poroelastic medium (e.g., Lubis et al., 2012; Jha and Juanes, 2014; Torberntsson et al., 2018; Norbeck et al., 2018; Noda, 2022; Heimisson and Rinaldi, 2022; Heimisson et al., 2022). Hydrogel frictional experiments have also unveiled intriguing slip phenomena, such as the spontaneous emergence of slow slip pulses (e.g., Galeano et al., 2000; Baumberger et al., 2002; Ronsin et al., 2011). Such observations are postulated to be linked to the poroelastic properties of these gels, potentially sharing origins with slow slip events observed on terrestrial faults (Heimisson et al., 2019).

Broadly speaking, understanding the intricacies of thin fluid-bearing layers – whose lateral extent significantly exceeds their thickness – is essential in fields like geomechanics, hydrology, reservoir applications, and soft matter physics. The 'thin layer' conceptualization serves not only as a valuable tool for characterizing fault zones and frictional interfaces in the realm of poroelastic behavior but also finds relevance in areas such as gas reservoirs, aquifers, and gels (e.g., Smith et al., 2022; Alghamdi et al., 2020; Yoon et al., 2010). As touched upon earlier, boundary integral methods shine in elucidating the deformation and mechanics of frictional, fracturing, and other interface challenges, which can be conceptualized as thin layers with infinitesimal width. Nevertheless, boundary integral techniques can be extended to layers with finite thickness, provided the essential separation of scales remains intact.

As previously mentioned, the theory of poroelasticity has been applied in various contexts, either to represent the bulk surrounding an interface or fracture or around a thin layer. Given this, it is understandable that several boundary integral and dislocation approaches have emerged (e.g., Rice and Cleary, 1976; Cheng and Liggett, 1984; Cheng and Detournay, 1988; Atkinson and Craster, 1991; Cheng and Detournay, 1998; Song and Rudnicki, 2017). A notable challenge in deriving and applying these solutions lies in the assumptions made about pore pressure at the sliding/fracture interface or the thin layer interface. Commonly, assumptions of no flux across the interface or continuous pressure are made. These assumptions implicitly suggest that the interface is either impermeable or that it equilibrates pressure instantaneously, respectively (Heimisson et al., 2019). In many pertinent applications, the interface or thin layers might possess their own hydraulic structure. Song and Rudnicki (2017) tackled this by examining a plane strain dislocation on a leaky interface where pressure can equilibrate over a finite duration. To feasibly characterize this leaky interface, a linear approximation of the pressure in the interface/layer is made. Song and Rudnicki (2017)'s analysis did not account for potential internal pressurization or depressurization within the interface/layer. Expanding on their work, Heimisson et al. (2021) introduced a bi-linear approximation (detailed in Section 2.2) that permits the interface/layer to undergo pressurization or depressurization. This approximation was subsequently integrated into a plane-strain SBIM for faulting and fracturing in a poroelastic solid Heimisson et al. (2022). To the author's best knowledge, this was among the earliest derivations of an SBIM for a poroelastic medium—a somewhat unexpected development considering the success of this approach in elastic mediums. Another derivation was by Noda (2022), who utilized the plane strain space–time domain boundary integral solutions from Cheng and Detournay (1988) and applied Fourier transforms along the spatial dimension of the fracture interface, thereby achieving an SBI representation of a poroelastic bulk. However, this method adopts the boundary conditions from Cheng and Detournay (1988), which mandates the interface pressure to be zero, thus constraining the solution's broader applicability.

In this work, I build upon the studies of Heimisson et al. (2021, 2022) by deriving SBI solutions for a planar interface/layer within a 3D poroelastic medium. This interface is capable of undergoing simultaneous Mode I, II, and III displacements. Additionally, processes leading to the internal pressurization or depressurization of the layer are considered. While I focus on the applications of the solutions based on a bi-linear pressure profile, I acknowledge that this approximation does not lend itself to studies that

carry out detailed modeling of the internal dynamic of the thin layer. I thus also introduce more generalized solutions that assume arbitrary pressurization or fluid flux at the interface boundaries, thereby accommodating asymmetric pressure or flux scenarios. These spectral boundary integral equations have not been published before in either 2D or 3D. I demonstrate that the bi-linear representation can be simplified to either the arbitrary pore pressure scenario or the arbitrary fluid flux scenario, contingent upon a single non-dimensional parameter present in all stress–displacement relations, however novel terms, without an correspondence to the bi-linear pressure solution, arise in stress-flux or pressurization relationships and pressure or flux equations.

2. Theory

2.1. Linear poroelasticity

Before delving into the specifics of our problem setup, which will be detailed in Section 2.2, it is essential to first understand the foundational theory of poroelasticity. A particularly intuitive representation of the Biot theory of quasi-static poroelasticity is the Navier form of the governing equations. Presented compactly in index notation, these can be expressed as (e.g. Detournay and Cheng, 1995; Cheng, 2016):

$$Gu_{i,kk} + \frac{G}{1-2v}u_{k,ki} = \alpha p_{,i} \tag{1}$$

and

$$\frac{1}{M}p_{,t} - \kappa p_{,kk} = -\alpha u_{k,kt}, \tag{2}$$

In Eq. (1), the left-hand side mirrors the theory of quasi-static elasticity, characterized by the shear modulus G and Poisson's ratio v. Notably, in poroelasticity, this ratio is referred to as the drained Poisson's ratio. The right-hand side introduces a source term dependent on the spatial derivative of pore pressure, with its magnitude determined by α, the Biot coefficient, which ranges between 0 and 1. It is crucial to recognize that p, representing pore pressure, is consistently interpreted as a deviation from equilibrium in a fully saturated porous medium, allowing it to assume both negative and positive values.

Eq. (2), on the other hand, represents a standard diffusion equation complemented by a source term. This equation establishes the conventional definition of hydraulic diffusivity in poroelasticity as $c = M\kappa$. Here, κ denotes mobility, defined as the ratio of permeability to dynamic fluid viscosity, and thus possesses units of $m^2/Pa\ s$. M represents the less commonly referenced Biot modulus, defined at a constant volumetric strain as the fluid volume change per unit pressure change. The right-hand side of Eq. (2) introduces an additional source term associated with volumetric strain. Consequently, the right-hand sides of the aforementioned equations introduce significant complexity to any solution strategy, extending beyond the realms of mere porous media flow or elasticity due to their two-way coupling. It is worth noting that, unlike in the analogous theory of thermoelasticity, simply decoupling by neglecting one of the right-hand sides does not yield an accurate approximation in most cases.

Eq. (2) can be recast in terms of ζ, representing the fluid mass content:

$$\zeta_{,t} - c'\zeta_{,kk} = 0, \tag{3}$$

This equation takes the form of another diffusion equation, defining an additional hydraulic diffusivity, c'. Historically, c' is referred to as the consolidation coefficient. It can be expressed in terms of mobility and the storage coefficient S as $c' = \kappa/S$. The relationship between the two diffusion coefficients is given by:

$$c' = c\frac{(1-2v_u)(1-v)}{(1-2v)(1-v_u)}. \tag{4}$$

Here, v_u denotes the undrained Poisson's ratio, which can be expressed in terms of the parameters introduced earlier:

$$v_u = \frac{2Gv + M\alpha^2(1-2v)}{2G + 2M\alpha^2(1-2v)}. \tag{5}$$

While c might be more intuitive for many readers, given the frequent use in studies on pressure diffusion, we will predominantly present results in terms of c', as it leads to more concise equations. Nonetheless, it is important to highlight that the values of the two diffusivities are typically comparable.

For more streamlined expressions, we introduce Skempton's coefficient:

$$B = \frac{3M\alpha(1-2v)}{2G(1+v) + 3M\alpha^2(1-2v)}. \tag{6}$$

This coefficient correlates the change in pore pressure with the change in volumetric stress under undrained conditions. Additionally, B and v_u share the following relationship:

$$B = \frac{3(v_u - v)}{\alpha(1-2v)(1+v_u)}. \tag{7}$$

In the subsequent discussions, we will generally describe poroelasticity and the boundary integral solutions in terms of G, B, v, and v_u, which collectively define the mechanical properties of the medium. For the description of fluid-flow or hydraulic properties, we will use either c, c', or κ. To summarize, we have the relationships $\kappa = c/M = c'S$ and the following useful equations:

$$S = \frac{9(v_u - v)(1 - v_u)}{2B^2G(1-v)(1+v_u)^2} \tag{8}$$

$$M = \frac{2B^2 G(1 - 2\nu)(1 + \nu_u)^2}{9(1 - 2\nu_u)(\nu_u - \nu)} \tag{9}$$

2.2. Problem setup

Consider two identical isotropic linear quasi-static poroelastic half-spaces occupying the regions $z > 0$ and $z < 0$ within a 3D domain, as illustrated in Fig. 1a. These half-spaces are separated by a thin layer extending from $z = \epsilon$ to $z = -\epsilon$ (Fig. 1b-d).

In the forthcoming analysis, we assume $\epsilon \to 0$, implying that the interface has an infinitesimal thickness. This assumption is appropriate for analyzing a perfectly planar dislocation. However, it is important to note that solutions for a finite layer ($\epsilon > 0$) can be well approximated by these results, provided that the inequalities $k_x \epsilon \ll 1$ and $k_y \epsilon \ll 1$ hold for all k_x and k_y in the x, y plane at $z = 0$. Here, k_x and k_y represent the wavenumbers, inversely proportional to wavelengths (e.g., $k_x = 2\pi/\lambda_x$). In simpler terms, for all non-zero Fourier coefficients in a 2D spatial Fourier series representation of the fields, the conditions $k_x \epsilon \ll 1$ and $k_y \epsilon \ll 1$ must be satisfied.

In certain cases of implementing boundary conditions, we explicitly describe ϵ (Fig. 1d). This approach can be viewed as a boundary layer solution, where the outer solution assumes an infinitesimal layer, while the inner solution accounts for a finite width, akin to the methodology in Rudnicki and Rice (2006, Appendix B). Nevertheless, all solutions can be approximately applied to thin layer problems, which is crucial for three main reasons: First, in reality, interfaces, even highly localized shear cracks, possess a finite thickness. Second, problems involving thin layers, where the $k_x \epsilon \ll 1$ and $k_y \epsilon \ll 1$ separation of scales occurs, are quite common, as highlighted in the introduction. Finally, in scenarios where pore pressure and slip are coupled, variations in pore pressure and fluid flux can occur over extremely small length scales (e.g., Rice et al., 2014; Platt et al., 2014; Heimisson et al., 2021, 2022). Thus, a versatile idealization of the shear zone as a thin layer is indispensable for upscaling and comprehending the impact of small shear zone processes on large scale slip.

We introduce three distinct solutions based on the applied boundary conditions related to pressure and fluid flow, detailed explicitly in Section 2.4. The first solution allows for arbitrary pore pressure on either side of the thin layer/interface, with the pressures $(p^+(x, y, t), p^-(x, y, t))$ not necessarily being identical (as shown in Fig. 1b). The second solution permits arbitrary volumetric fluid flux on either side of the thin layer/interface ($J^+(x, y, t), J^-(x, y, t)$), again without the need for pressures on both sides to match (illustrated in Fig. 1c). The final solution describes the pressure inside the shear zone using the following equations:

$$
\begin{aligned}
p(x, y, z, t) &= \frac{z}{\epsilon}(p^+(x, y, t) - p_c(x, y, t)) + p_c(x, y, t) \quad \text{if } 0 < z < \epsilon \\
p(x, y, z, t) &= \frac{z}{\epsilon}(p_c(x, y, t) - p^-(x, y, t)) + p_c(x, y, t) \quad \text{if } -\epsilon < z < 0.
\end{aligned}
\tag{10}
$$

This methodology can be likened to a boundary layer solution. While the outer solution treats the layer as infinitesimal, the inner solution acknowledges its finite width, drawing parallels to the approach in Rudnicki and Rice (2006, Appendix B). In this context, p_c denotes the pressure at the center of the layer ($z = 0$). Leveraging the pressure distribution, we can implement a pressure-dependent flux boundary condition derived from Darcy's law:

$$\frac{dp^\pm}{dz}\bigg|_{z=0^\pm} = \pm \frac{\kappa_c}{\kappa} \frac{(p^\pm(x, y, t) - p_c(x, y, t))}{\epsilon} \tag{11}$$

Here, κ_c represents the assumed mobility (the ratio of permeability to dynamic viscosity) for fluid movement across the layer in the z direction. This boundary condition aims to incorporate fundamental aspects of the thin layer physics into the SBI. It is noteworthy that when $p_c = 0$, the bilinear boundary condition is identical the leaky layer model presented by Song and Rudnicki (2017).

2.3. Solution strategy

Rather than directly addressing the governing equations in their explicit and coupled form ((1), (2)), we adopt a strategy that employs a decoupled system of equations. We leverage the displacement functions initially introduced by McNamee and Gibson (1960) for plane-strain deformation, which were later expanded to 3D by Schiffman and Fungaroli (1965). The formalism was further extended to account for compressible fluids with minor modifications by Verruijt (1971). In this work, we adhere to the relations as detailed by Cheng (2016, pages 225–226).

In essence, McNamee and Gibson (1960), Schiffman and Fungaroli (1965), Verruijt (1971) demonstrated that solving the governing equations can be equated to addressing a bi-harmonic diffusion equation:

$$\frac{\partial}{\partial t}\left(\nabla^2 \mathcal{E}\right) - c'\nabla^4 \mathcal{E} = 0 \tag{12}$$

Accompanied by two Laplace's equations:

$$\nabla^2 S = 0 \text{ and } \nabla^2 Q = 0. \tag{13}$$

Subsequently, the relationships outlined by Cheng (2016, chapter 6.6.3) facilitate the transformation of these displacement functions, namely $\mathcal{E}$, S, and Q, into tangible fields, such as displacements and pore pressure.
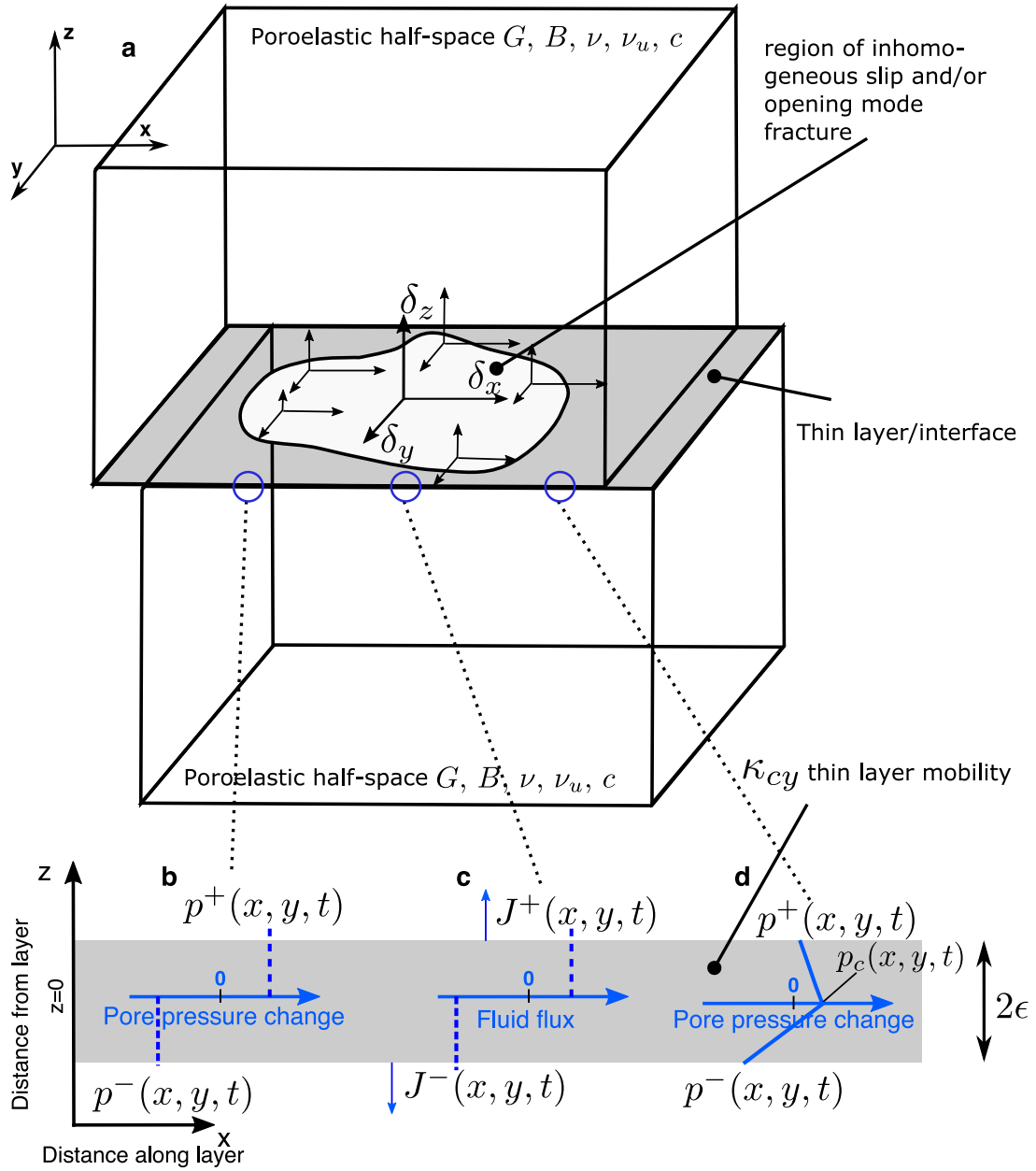
Fig. 1. Schematic representation of the problem setup. **a** Depicts two linear isotropic poroelastic half-spaces with identical material properties, separated by a thin layer or interface at $z = 0$. The interface, which may be considered as having a finite dimension in the z direction if its half-thickness ϵ is much smaller than the wavelength of any field in the x, y plane (thin layer), can undergo homogeneous and/or inhomogeneous Mode I fracture mode or slip in either x or y direction. Three distinct boundary integral solutions are presented, each differing in pore pressure boundary conditions at the interface. **b** Prescribes pore pressure on either side ($p^+(x, y, t)$ and $p^-(x, y, t)$). **c** Specifies volumetric flux on either side ($J^+(x, y, t)$ and $J^-(x, y, t)$). **d** Assumes a bi-linear pressure profile within the thin layer.

Our solution strategy begins with the introduction of the combined Laplace - 2D Fourier transform, defined as:

$$\bar{\bar{\delta}}_x(s, k_x, k_y) = \int_0^\infty \int_{-\infty}^\infty \int_{-\infty}^\infty \delta_x(t, x, y) e^{-ik_x x - ik_y y - st} \, dx \, dy \, dt \tag{14}$$

Here, the transform is applied to the slip or displacement discontinuity across the layer/interface in the x direction, as illustrated in Fig. 1 (further elaborated in the subsequent section).

By applying the Laplace - 2D Fourier transform to Eqs. (12) and (13), we obtain ordinary differential equations. These can be straightforwardly solved in both the upper and lower half-spaces (as depicted in Fig. 1), yielding:

$$\bar{\tilde{\mathcal{E}}}^{\pm} = C_1^{\pm} \exp(\pm ky) + C_2^{\pm} \exp(\pm k\sqrt{1 + s/(c'k^2)}y), \tag{15}$$

$$\bar{\tilde{S}}^{\pm} = C_3^{\pm} \exp(\pm ky), \tag{16}$$

$$\bar{\tilde{Q}}^{\pm} = C_4^{\pm} \exp(\pm ky). \tag{17}$$

After eliminating terms that diverge at infinity, the superscript $\pm$ denotes the upper and lower half-space, respectively. The constants C will be defined by the boundary conditions. The term $k = \sqrt{k_x^2 + k_y^2}$ represents the length of the wavenumber vector. In the transform domain, these solutions can be connected to displacements and pressure by transforming the relations provided by Cheng (2016, chapter 6.6.3):

$$\bar{\tilde{u}}_x^{\pm} = -ik_x\bar{\tilde{\mathcal{E}}}^{\pm} + ik_x z\bar{\tilde{S}}^{\pm} + 2ik_y\bar{\tilde{Q}}^{\pm}, \tag{18}$$

$$\bar{\tilde{u}}_y^{\pm} = -ik_y\bar{\tilde{\mathcal{E}}}^{\pm} + ik_y z\bar{\tilde{S}}^{\pm} - 2ik_x\bar{\tilde{Q}}^{\pm}, \tag{19}$$

$$\bar{\tilde{u}}_z^{\pm} = -\frac{\partial \bar{\tilde{\mathcal{E}}}^{\pm}}{\partial z} + z\frac{\partial \bar{\tilde{S}}^{\pm}}{\partial z} - (3 - 4v_u)\bar{\tilde{S}}^{\pm}, \tag{20}$$

$$\bar{\tilde{p}}^{\pm} = -G\frac{2(1-v)}{\alpha(1-2v)}\left[-k^2\bar{\tilde{\mathcal{E}}}^{\pm} + \frac{\partial^2 \bar{\tilde{\mathcal{E}}}^{\pm}}{\partial y^2} - \frac{2(v_u - v)}{1-v}\frac{\partial \bar{\tilde{S}}^{\pm}}{\partial y}\right]. \tag{21}$$

Other expressions, such as those for stresses or flux, can be derived from the above using Hooke's law or Darcy's law. For a more comprehensive list, refer to Cheng (2016, chapter 6.6.3), albeit not in the transform domain.

2.4. Boundary conditions

In this section, we outline the standard boundary conditions employed across all the spectral boundary integral solutions.

$$\lim_{z\to\pm\infty} u_x^{\pm}(x, y, z, t) = 0, \tag{22}$$

$$\lim_{z\to\pm\infty} u_y^{\pm}(x, y, z, t) = 0, \tag{23}$$

$$\lim_{z\to\pm\infty} u_z^{\pm}(x, y, z, t) = 0, \tag{24}$$

$$\lim_{z\to\pm\infty} p^{\pm}(x, y, z, t) = 0, \tag{25}$$

$$\lim_{z\to0} u_x^+(x, y, z, t) - u_x^-(x, y, z, t) = \delta_x(x, y, t), \tag{26}$$

$$\lim_{z\to0} u_y^+(x, y, z, t) - u_y^-(x, y, z, t) = \delta_y(x, y, t), \tag{27}$$

$$\lim_{z\to0} u_z^+(x, y, z, t) - u_z^-(x, y, z, t) = \delta_z(x, y, t), \tag{28}$$

$$\lim_{z\to0} \sigma_{xz}^+(x, y, z, t) - \sigma_{xz}^-(x, y, z, t) = 0, \tag{29}$$

$$\lim_{z\to0} \sigma_{yz}^+(x, y, z, t) - \sigma_{yz}^-(x, y, z, t) = 0, \tag{30}$$

$$\lim_{z\to0} \sigma_{zz}^+(x, y, z, t) - \sigma_{zz}^-(x, y, z, t) = 0, \tag{31}$$

The initial four conditions ensure that all fields diminish to zero at infinity, implying that the solutions are suitable for a full space. These conditions are inherently incorporated into the Displacement functions $\mathcal{E}$, S, and Q by excluding terms that diverge at infinity.

The subsequent three conditions establish arbitrary displacement discontinuities at the layer or interface boundaries. Specifically, $\delta_x(x, y, t)$ represents slip in the x direction, $\delta_y(x, y, t)$ indicates slip in the y direction, and $\delta_z(x, y, t)$ denotes the opening or closing (Mode I) of the interface (refer to Fig. 1 for visualization).

The last three of the boundary conditions ensures the continuity of traction across the layer or interface. When applying the boundary integral solutions to a scenario with a finite layer, this condition necessitates that the layer is sufficiently thin, as indicated by the conditions $k_x\epsilon \ll 1$ and $k_y\epsilon \ll 1$. Moreover, this assumption suggests that the layer's inertia can be disregarded, as noted by Rice et al. (2014). See some discussion of inertial effects in the discussion Section 5.1.

For a distinct solution, two additional boundary conditions are essential. In this context, we delve into the modification of boundary conditions based on the characterization of pore pressure or flux.

2.4.1. General pressure
The general pressure boundary condition can be expressed as:

$$\lim_{z\to0^+} p^+(x, y, z, t) = p_b^+(x, y, t), \tag{32}$$

$$\lim_{z \to 0^-} p^-(x, y, z, t) = p_b^-(x, y, t), \tag{33}$$

Here, the subscript $_b$ is introduced to emphasize that the boundary pressure field is a predefined condition and is not a variable in the solution. However, it is pertinent to mention that one could determine these pressure values using an alternative approach. This type of boundary condition might be particularly relevant when modeling phenomena like propagating hydraulic fractures, where the pressure at the fluid boundaries interacts with the response of the surrounding poroelastic medium.

2.4.2. General flux

The flux boundary condition can be defined as:

$$\lim_{z \to 0^+} -\kappa \frac{\partial}{\partial z} p^+(x, y, z, t) = J^+(x, y, t), \tag{34}$$

$$\lim_{z \to 0^-} -\kappa \frac{\partial}{\partial z} p^-(x, y, z, t) = J^-(x, y, t), \tag{35}$$

In this scenario, we assume that the volumetric fluid flux on either side of the layer can be both asymmetric and arbitrary. Such boundary conditions might be employed when the layer is conceptualized as a porous medium, allowing for the internal pressure gradient and flux into the bulk to be synchronized and interconnected.

2.4.3. Bi-linear pressure profile

While the general flux and pore pressure conditions necessitate that the fluid flux or pore pressure fields of the layer/interface are either known or imposed externally, there are alternative approaches. One such method involves deriving these conditions by addressing another internal problem, such as explicitly simulating flow within a hydraulic fracture or modeling porous media flow within a thin layer. The bi-linear pressure profile, as detailed in Eq. (11), serves as an approximation of this latter method. This approximation is valid under the conditions where the flux across the layer adheres to Darcy's law, and the pressure distribution closely aligns with the representation in Eq. (10).

As demonstrated by Heimisson et al. (2022), this bi-linear approximation facilitates a dimensional reduction in the simulation of the layer. Specifically, this means that the internal problem can be simplified to address a two-dimensional (x, y) domain, eliminating the need to solve for a more complex domain (x, y, z) where $-\epsilon < z < \epsilon$. In the study by Heimisson et al. (2022), which focused on a plane strain problem, the internal domain was effectively reduced from 2D to 1D. In such scenarios, p_c can be the primary pressure variable to solve for, from which the values of $p^\pm$ can subsequently be determined.

2.5. Solutions in Fourier-Laplace domain

In this section, we apply the boundary conditions outlined in the preceding section to determine the eight unknown constants, $C_{1-4}^\pm$, that emerge when solving for the displacement functions for each set of pressure or flux boundary conditions. To manage the algebraic complexity, we employ Matlab's symbolic manipulator. To validate the solutions, we insert them into the Navier form of the governing Eqs. (1) and (2) within the combined Laplace - 2D Fourier domain.

The subsequent step, after obtaining the solution in the Laplace - 2D Fourier domain, is to set $z = 0$ or apply the appropriate limit for fields that might exhibit discontinuities, such as pore pressure. This action significantly streamlines the expressions, enabling the analytical inversion of the Laplace transform. As a result, the known values are confined to the layer/interface plane. This approach aligns with common practices in other spectral boundary integral methodologies (Geubelle and Rice, 1995). Notable exceptions exist, such as in simulations of parallel faults (Barbot, 2021) or off-fault responses where the Laplace transform is inverted numerically (Heimisson and Rinaldi, 2022). However, it is essential to emphasize that having knowledge of the field at the interface/layer boundaries allows for efficient mapping, for instance, from slip to stress or from slip to pore pressure, or from flux to stress. This capability is invaluable for addressing a wide range of pertinent physical problems where such relationships are crucial.

Before delving into the Laplace–Fourier solution, we first explore mathematical functions that consistently appear across most solutions. These functions pertain to convolution kernels in the time-Fourier domain and account for the temporal evolution resulting from fluid diffusion.

In the Bi-linear pressure diffusion problem, the functions below emerge:

$$\bar{H}_1(s, k) = 1 - \frac{2(\nu_u - \nu)}{1 - \nu} \frac{c'k^2}{s} \frac{1 + \mathcal{F}}{\mathcal{F} + \sqrt{1 + s/c'k^2}} \left(\sqrt{1 + s/c'k^2} - 1 \right), \tag{36}$$

and

$$\bar{H}_2(s, k) = \frac{\sqrt{1 + s/c'k^2} - 1}{\sqrt{1 + s/c'k^2} + \mathcal{F}}, \tag{37}$$

where $\mathcal{F}$ is a dimensionless group that characterizes the importance of flux across the layer:

$$\mathcal{F} = \frac{\kappa_c}{\kappa} \frac{1}{k\epsilon}. \tag{38}$$

The functions $\bar{H}_1(s,k)$ and $\bar{H}_2(s,k)$ bear a striking resemblance to the corresponding functions presented by Heimisson et al. (2022), albeit for a plane strain problem with a bi-linear pressure distribution. It is important to emphasize that in this context, $k = \sqrt{k_x^2 + k_y^2}$. However, in scenarios where either k_x or $k_y = 0$, these equations revert to the plane-strain limit, as anticipated.

In the undrained limit (characterized by a low c' or short time duration), both $\bar{H}_1$ and $\bar{H}_2$ approach 1. However, these functions also exhibit other notable limiting cases. For instance, when $\mathcal{F} = 0$, the layer acts as an impenetrable barrier to flow. Conversely, as $\mathcal{F} \to \infty$, the layer becomes highly permeable or poses no resistance to flow. This could occur, for example, if the layer's thickness $\epsilon \to 0$, allowing for instantaneous pressure equilibration.

These limiting cases will be further explored in the context of the general pressure boundary condition and the general flux boundary condition. Specifically, the Laplace–Fourier representation of the convolution kernels for the general flux (as discussed in Section 2.4.2) is related to the Bi-linear boundary condition (as detailed in Section 2.4.3) when $\mathcal{F} = 0$.

In the special case where $\mathcal{F} = 0$, the functions $\bar{H}_1$ and $\bar{H}_2$ simplify to:

$$\bar{H}_1(\mathcal{F} = 0) = 1 - \frac{2(v_u - v)}{1 - v}\frac{c'k^2}{s}\frac{\sqrt{1 + s/c'k^2} - 1}{\sqrt{1 + s/c'k^2}}, \tag{39}$$

$$\bar{H}_2(\mathcal{F} = 0) = \frac{\sqrt{1 + s/c'k^2} - 1}{\sqrt{1 + s/c'k^2}}. \tag{40}$$

Conversely, in the limit as $\mathcal{F} \to \infty$, which corresponds to the scenario where the layer becomes highly permeable, the functions $\bar{H}_1$ and $\bar{H}_2$ are given by:

$$\bar{H}_1(\mathcal{F} \to \infty) = 1 - \frac{2(v_u - v)}{1 - v}\frac{c'k^2}{s}\left(\sqrt{1 + s/c'k^2} - 1\right), \tag{41}$$

$$\bar{H}_2(\mathcal{F} \to \infty) = 0. \tag{42}$$

Additionally, we introduce another kernel, $\bar{H}_3$, defined as:

$$\bar{H}_3 = \frac{1}{\bar{H}_2(\mathcal{F} = 0) - 1} = -\sqrt{1 + s/c'k^2}. \tag{43}$$

This kernel, $\bar{H}_3$, emerges in a specific relationship used to calculate flux within the context of the general pore pressure boundary condition.

Next, we present the spectral boundary integral solutions corresponding to the three boundary conditions related to pressure and flux, as detailed in sections 2.4.1, 2.4.2, and 2.4.3.

2.6. General pore pressure

The stress components relevant to the plane of the layer are:

$$\bar{\tilde{\sigma}}_{xz} = -\frac{G\bar{\tilde{\delta}}_x}{2k}\left(k_x^2\frac{\bar{H}_1(\mathcal{F} \to \infty)}{1 - v_u} + k_y^2\right) + \frac{G\bar{\tilde{\delta}}_y k_x k_y}{2k}\left(1 - \frac{\bar{H}_1(\mathcal{F} \to \infty)}{1 - v_u}\right) + \cdots$$
$$+ \frac{ik_x}{k}\frac{3}{4B(1 + v_u)}(\bar{\tilde{p}}_b^+ - \bar{\tilde{p}}_b^-)\left(\bar{H}_1(\mathcal{F} \to \infty) - 1\right), \tag{44}$$

$$\bar{\tilde{\sigma}}_{yz} = \frac{G\bar{\tilde{\delta}}_x k_x k_y}{2k}\left(1 - \frac{\bar{H}_1(\mathcal{F} \to \infty)}{1 - v_u}\right) - \frac{G\bar{\tilde{\delta}}_y}{2k}\left(k_y^2\frac{\bar{H}_1(\mathcal{F} \to \infty)}{1 - v_u} + k_x^2\right) + \cdots$$
$$+ \frac{ik_y}{k}\frac{3}{4B(1 + v_u)}(\bar{\tilde{p}}_b^+ - \bar{\tilde{p}}_b^-)\left(\bar{H}_1(\mathcal{F} \to \infty) - 1\right), \tag{45}$$

$$\bar{\tilde{\sigma}}_{zz} = -\frac{Gk\bar{\tilde{\delta}}_z}{2(1 - v_u)}\bar{H}_1(\mathcal{F} \to \infty) + \frac{3}{4B(1 + v_u)}(\bar{\tilde{p}}_b^+ + \bar{\tilde{p}}_b^-)\left(\bar{H}_1(\mathcal{F} \to \infty) - 1\right). \tag{46}$$

In this scenario, we have $\bar{\tilde{p}}^\pm = \bar{\tilde{p}}_b^\pm$. However, it may be beneficial to have an expression that provides the volumetric fluid flux in and out of the layer in the z direction.

$$\bar{\tilde{J}}^\pm = -\frac{ik_x GBk\kappa\bar{\tilde{\delta}}_x}{3}\frac{1 + v_u}{1 - v_u}(1 + \bar{H}_3) - \frac{ik_y GBk\kappa\bar{\tilde{\delta}}_y}{3}\frac{1 + v_u}{1 - v_u}(1 + \bar{H}_3)$$
$$\pm \frac{kGBk\kappa\bar{\tilde{\delta}}_z}{3}\frac{1 + v_u}{1 - v_u}(1 + \bar{H}_3) \mp \bar{\tilde{p}}_b^\pm k\kappa\bar{H}_3. \tag{47}$$

2.7. General flux

The stress components relevant to the plane of the layer are:

$$
\bar{\bar{\sigma}}_{xz} = -\frac{G\bar{\bar{\delta}}_x}{2k}\left(k_x^2\frac{\bar{H}_1(\mathcal{F}=0)}{1-\nu_u}+k_y^2\right)+\frac{G\bar{\bar{\delta}}_y k_x k_y}{2k}\left(1-\frac{\bar{H}_1(\mathcal{F}=0)}{1-\nu_u}\right)+\cdots
$$
$$
\frac{ik_x}{k^2}\frac{3}{4B\kappa(1+\nu_u)}(\bar{\bar{J}}^+ + \bar{\bar{J}}^-)\left(\bar{H}_1(\mathcal{F}=0)-1\right),
\tag{48}
$$

$$
\bar{\bar{\sigma}}_{yz} = \frac{G\bar{\bar{\delta}}_x k_x k_y}{2k}\left(1-\frac{\bar{H}_1(\mathcal{F}=0)}{1-\nu_u}\right)-\frac{G\bar{\bar{\delta}}_y}{2k}\left(k_y^2\frac{\bar{H}_1(\mathcal{F}=0)}{1-\nu_u}+k_x^2\right)+\cdots
$$
$$
\frac{ik_y}{k^2}\frac{3}{4B\kappa(1+\nu_u)}(\bar{\bar{J}}^+ + \bar{\bar{J}}^-)\left(\bar{H}_1(\mathcal{F}=0)-1\right),
\tag{49}
$$

$$
\bar{\bar{\sigma}}_{zz} = -\frac{Gk\bar{\bar{\delta}}_z}{2(1-\nu_u)}\bar{H}_1(\mathcal{F}=0)+\frac{1}{k}\frac{3}{4B\kappa(1+\nu_u)}(\bar{\bar{J}}^+ - \bar{\bar{J}}^-)\left(\bar{H}_1(\mathcal{F}=0)-1\right).
\tag{50}
$$

The pore pressure at the layer boundaries is:

$$
\bar{\bar{p}}^\pm = \mp\frac{ik_x GB\bar{\bar{\delta}}_x}{3}\frac{1+\nu_u}{1-\nu_u}\bar{H}_2(\mathcal{F}=0)\mp\frac{ik_y GB\bar{\bar{\delta}}_y}{3}\frac{1+\nu_u}{1-\nu_u}\bar{H}_2(\mathcal{F}=0)
$$
$$
+\frac{kGB\bar{\bar{\delta}}_z}{3}\frac{1+\nu_u}{1-\nu_u}\bar{H}_2(\mathcal{F}=0)\mp\frac{\bar{\bar{J}}^\pm}{k\kappa}\left(\bar{H}_2(\mathcal{F}=0)-1\right).
\tag{51}
$$

2.8. Bi-linear pressure

The stress components relevant to the plane of the layer are:

$$
\bar{\bar{\sigma}}_{xz} = -\frac{G\bar{\bar{\delta}}_x}{2k}\left(k_x^2\frac{\bar{H}_1(s,k)}{1-\nu_u}+k_y^2\right)+\frac{G\bar{\bar{\delta}}_y k_x k_y}{2k}\left(1-\frac{\bar{H}_1(s,k)}{1-\nu_u}\right),
\tag{52}
$$

$$
\bar{\bar{\sigma}}_{yz} = -\frac{G\bar{\bar{\delta}}_y}{2k}\left(k_y^2\frac{\bar{H}_1(s,k)}{1-\nu_u}+k_x^2\right)+\frac{G\bar{\bar{\delta}}_x k_x k_y}{2k}\left(1-\frac{\bar{H}_1(s,k)}{1-\nu_u}\right),
\tag{53}
$$

$$
\bar{\bar{\sigma}}_{zz} = \bar{\bar{p}}_c\frac{3}{2B(1+\nu_u)}\frac{\mathcal{F}}{\mathcal{F}+1}(\bar{H}_1(s,k)-1)-\frac{Gk\bar{\bar{\delta}}_z}{2(1-\nu_u)}\bar{H}_1(s,k).
\tag{54}
$$

The pore pressure at the layer boundaries is:

$$
\bar{\bar{p}}^\pm = \mp\frac{ik_x GB\bar{\bar{\delta}}_x}{3}\frac{1+\nu_u}{1-\nu_u}\bar{H}_2(s,k)\mp\frac{ik_y GB\bar{\bar{\delta}}_y}{3}\frac{1+\nu_u}{1-\nu_u}\bar{H}_2(s,k)
$$
$$
-\bar{\bar{p}}_c\frac{\mathcal{F}}{\mathcal{F}+1}\left(\bar{H}_2(s,k)-1\right)+\frac{kGB\bar{\bar{\delta}}_z}{3}\frac{1+\nu_u}{1-\nu_u}\bar{H}_2(s,k).
\tag{55}
$$

Comparing the Bi-linear pressure expressions above to those derived in Heimisson et al. (2021, 2022), it is evident that setting one wavenumber to 0 yields the plane-strain solutions, as anticipated.

While it turns out that all these expressions can be expressed in terms of the same $\bar{H}_{1-3}(s,k)$ functions for different limiting cases of $\mathcal{F}$, it is important to stress that the SBI equations for general pressure and flux are not just special limits of the bi-linear pressure. The reader can observe in the last term of Eqs. (44)–(46) and (48)–(50) that the stress depends on the pressure or flux. This is not the case for the Bi-linear pressure due to imposed symmetries. Further, $\bar{H}_3(s,k)$ has not correspondence in the bi-linear solution as far as the author can identify.

3. Fourier-time domain solutions

3.1. Laplace inversion

In this subsection, we focus on inverting the Laplace transform. Drawing parallels with Heimisson et al. (2022), we segregate the instantaneous undrained response from the transient poroelastic response by introducing:

$$
\bar{K}_1 = \bar{H}_1 - 1 \text{ and } \bar{K}_2 = \bar{H}_2 - 1.
\tag{56}
$$

While there is no need for a similar separation for $\bar{H}_3$, we define

$$
\bar{K}_3 = \bar{H}_3,
\tag{57}
$$

to maintain consistent notation.

The inverse transforms of $\bar{K}_1$ and $\bar{K}_2$ are provided by Heimisson et al. (2022). They only differ in the definition of k:

$$K_1(t,k) = -\frac{2(\nu_u - \nu)}{1-\nu}ck^2(1+\mathcal{F})\left(1 + \frac{1}{\mathcal{F}-1}\left[\mathcal{F}e^{(\mathcal{F}^2-1)ck^2t}\text{erfc}\left(\mathcal{F}\sqrt{ck^2t}\right) - \mathcal{F} + \text{erf}\left(\sqrt{ck^2t}\right)\right]\right),$$ (58)

$$K_2(t,k) = -ck^2(1+\mathcal{F})\left[\frac{e^{-ck^2t}}{\sqrt{\pi ck^2t}} - \mathcal{F}e^{(\mathcal{F}^2-1)ck^2t}\text{erfc}\left(\mathcal{F}\sqrt{ck^2t}\right)\right].$$ (59)

When considering the limits of $\mathcal{F} = 0$ and $\mathcal{F} \to \infty$, we can derive the corresponding limits from Eqs. (39) and (41):

$$K_1(\mathcal{F} = 0) = -\frac{2(\nu_u - \nu)}{1-\nu}ck^2\text{erfc}\left(\sqrt{ck^2t}\right),$$ (60)

$$K_1(\mathcal{F} \to \infty) = -\frac{2(\nu_u - \nu)}{1-\nu}ck^2\left(\frac{e^{-ck^2t}}{\sqrt{\pi ck^2t}} - \text{erfc}\left(\sqrt{ck^2t}\right)\right).$$ (61)

For Eq. (40), we have:

$$K_2(\mathcal{F} = 0) = -ck^2\frac{e^{-ck^2t}}{\sqrt{\pi ck^2t}},$$ (62)

However, the limit $K_2(\mathcal{F} \to \infty) = 0$.

Lastly, while the $K_3(t,k)$ kernel has not been previously published in this context, its inversion is straightforward:

$$K_3(t,k) = \frac{e^{-c'k^2t}}{2\sqrt{\pi}\sqrt{c'k^2}t^{3/2}},$$ (63)

3.2. Solutions

We now invert the Laplace transforms to the time domain using the convolution theorem and the kernels K_{1-3}. We list the corresponding solutions to those listed in sections 2.6, 2.7, and 2.8 here below. We thus arrive at the time-wavenumber domain representation of the spectral boundary integral.

3.3. General pore pressure

$$\hat{\sigma}_{xz} = -\frac{G}{2k}\left(\frac{k_x^2}{1-\nu_u}\left(\hat{\delta}_x + \int_0^t \hat{\delta}_x(t')K_1(\mathcal{F} \to \infty, t-t', k)dt'\right) + k_y^2\hat{\delta}_x\right)$$ (64)

$$+ \frac{Gk_xk_y}{2k}\left(\hat{\delta}_y - \frac{1}{1-\nu_u}\left(\hat{\delta}_y + \int_0^t \hat{\delta}_y(t')K_1(\mathcal{F} \to \infty, t-t', k)dt'\right)\right) + \cdots$$

$$+ \frac{ik_x}{k}\frac{3}{4B(1+\nu_u)}\int_0^t (\hat{p}_b^+(t') - \hat{p}_b^-(t'))K_1(\mathcal{F} \to \infty, t-t', k)dt',$$

$$\hat{\sigma}_{yz} = -\frac{G}{2k}\left(\frac{k_y^2}{1-\nu_u}\left(\hat{\delta}_y + \int_0^t \hat{\delta}_y(t')K_1(\mathcal{F} \to \infty, t-t', k)dt'\right) + k_x^2\hat{\delta}_y\right)$$ (65)

$$+ \frac{Gk_xk_y}{2k}\left(\hat{\delta}_x - \frac{1}{1-\nu_u}\left(\hat{\delta}_x + \int_0^t \hat{\delta}_x(t')K_1(\mathcal{F} \to \infty, t-t', k)dt'\right)\right) + \cdots$$

$$+ \frac{ik_y}{k}\frac{3}{4B(1+\nu_u)}\int_0^t (\hat{p}_b^+(t') - \hat{p}_b^-(t'))K_1(\mathcal{F} \to \infty, t-t', k)dt',$$

$$\bar{\hat{\sigma}}_{zz} = -\frac{Gk}{2(1-\nu_u)}\left(\hat{\delta}_z + \int_0^t \hat{\delta}_z(t')K_1(\mathcal{F} \to \infty, t-t', k)dt'\right)$$ (66)

$$+ \frac{3}{4B(1+\nu_u)}\int_0^t (\hat{p}_b^+(t') + \hat{p}_b^-(t'))K_1(\mathcal{F} \to \infty, t-t', k)dt',$$

$$\hat{J}^{\pm} = -\frac{ik_x GBk\kappa}{3}\frac{1+\nu_u}{1-\nu_u}\left(\hat{\delta}_x + \int_0^t \hat{\delta}_x(t')K_3(t-t', k)dt'\right)$$ (67)

$$- \frac{ik_y GBk\kappa}{3}\frac{1+\nu_u}{1-\nu_u}\left(\hat{\delta}_y + \int_0^t \hat{\delta}_y(t')K_3(t-t', k)dt'\right)$$

$$\pm \frac{kGBk\kappa}{3}\frac{1+\nu_u}{1-\nu_u}\left(\hat{\delta}_z + \int_0^t \hat{\delta}_z(t')K_3(t-t', k)dt'\right) \mp k\kappa\int_0^t \hat{p}_b^{\pm}(t')K_3(t-t', k)dt'.$$

3.4. General flux

$$\hat{\sigma}_{xz} = -\frac{G}{2k}\left(\frac{k_x^2}{1-\nu_u}\left(\hat{\delta}_x + \int_0^t \hat{\delta}_x(t')K_1(\mathcal{F}=0,t-t',k)dt'\right) + k_y^2\hat{\delta}_x\right)$$
$$+ \frac{Gk_xk_y}{2k}\left(\hat{\delta}_y - \frac{1}{1-\nu_u}\left(\hat{\delta}_y + \int_0^t \hat{\delta}_y(t')K_1(\mathcal{F}=0,t-t',k)dt'\right)\right) + \cdots$$
$$+ \frac{ik_x}{k}\frac{3}{4B\kappa(1+\nu_u)}\int_0^t (\hat{J}^+(t') + \hat{J}^-(t'))K_1(\mathcal{F}=0,t-t',k)dt', \tag{68}$$

$$\hat{\sigma}_{yz} = -\frac{G}{2k}\left(\frac{k_y^2}{1-\nu_u}\left(\hat{\delta}_y + \int_0^t \hat{\delta}_y(t')K_1(\mathcal{F}=0,t-t',k)dt'\right) + k_x^2\hat{\delta}_y\right)$$
$$+ \frac{Gk_xk_y}{2k}\left(\hat{\delta}_x - \frac{1}{1-\nu_u}\left(\hat{\delta}_x + \int_0^t \hat{\delta}_x(t')K_1(\mathcal{F}=0,t-t',k)dt'\right)\right) + \cdots$$
$$+ \frac{ik_y}{k}\frac{3}{4B\kappa(1+\nu_u)}\int_0^t (\hat{J}^+(t') + \hat{J}^-(t'))K_1(\mathcal{F}=0,t-t',k)dt', \tag{69}$$

$$\bar{\hat{\sigma}}_{zz} = -\frac{Gk}{2(1-\nu_u)}\left(\hat{\delta}_z + \int_0^t \hat{\delta}_z(t')K_1(\mathcal{F}=0,t-t',k)dt'\right)$$
$$+ \frac{1}{k}\frac{3}{4B\kappa(1+\nu_u)}\int_0^t (\hat{J}^+(t') - \hat{J}^-(t'))K_1(\mathcal{F}=0,t-t',k)dt', \tag{70}$$

$$\bar{\hat{p}}^{\pm} = \mp\frac{ik_xGB}{3}\frac{1+\nu_u}{1-\nu_u}\left(\hat{\delta}_x + \int_0^t \hat{\delta}_x(t')K_2(\mathcal{F}=0,t-t',k)dt'\right)$$
$$\mp\frac{ik_yGB}{3}\frac{1+\nu_u}{1-\nu_u}\left(\hat{\delta}_y + \int_0^t \hat{\delta}_y(t')K_2(\mathcal{F}=0,t-t',k)dt'\right)$$
$$+ \frac{kGB}{3}\frac{1+\nu_u}{1-\nu_u}\left(\hat{\delta}_z + \int_0^t \hat{\delta}_z(t')K_2(\mathcal{F}=0,t-t',k)dt'\right) \mp \frac{1}{k\kappa}\int_0^t \hat{J}^{\pm}(t')K_2(\mathcal{F}=0,t-t',k)dt'. \tag{71}$$

3.5. Bi-linear pressure

$$\hat{\sigma}_{xz} = -\frac{G}{2k}\left(\frac{k_x^2}{1-\nu_u}\left(\hat{\delta}_x + \int_0^t \hat{\delta}_x(t')K_1(t-t',k)dt'\right) + k_y^2\hat{\delta}_x\right)$$
$$+ \frac{Gk_xk_y}{2k}\left(\hat{\delta}_y - \frac{1}{1-\nu_u}\left(\hat{\delta}_y + \int_0^t \hat{\delta}_y(t')K_1(t-t',k)dt'\right)\right), \tag{72}$$

$$\hat{\sigma}_{yz} = -\frac{G}{2k}\left(\frac{k_y^2}{1-\nu_u}\left(\hat{\delta}_y + \int_0^t \hat{\delta}_y(t')K_1(t-t',k)dt'\right) + k_x^2\hat{\delta}_y\right)$$
$$+ \frac{Gk_xk_y}{2k}\left(\hat{\delta}_x - \frac{1}{1-\nu_u}\left(\hat{\delta}_x + \int_0^t \hat{\delta}_x(t')K_1(t-t',k)dt'\right)\right), \tag{73}$$

$$\bar{\hat{\sigma}}_{zz} = -\frac{Gk}{2(1-\nu_u)}\left(\hat{\delta}_z + \int_0^t \hat{\delta}_z(t')K_1(t-t',k)dt'\right)$$
$$+ \frac{3}{2B(1+\nu_u)}\frac{\mathcal{F}}{\mathcal{F}+1}\int_0^t \hat{p}_c(t')K_1(t-t',k)dt', \tag{74}$$

$$\bar{\hat{p}}^{\pm} = \mp\frac{ik_xGB}{3}\frac{1+\nu_u}{1-\nu_u}\left(\hat{\delta}_x + \int_0^t \hat{\delta}_x(t')K_2(t-t',k)dt'\right)$$
$$\mp\frac{ik_yGB}{3}\frac{1+\nu_u}{1-\nu_u}\left(\hat{\delta}_y + \int_0^t \hat{\delta}_y(t')K_2(t-t',k)dt'\right) \tag{75}$$
$$+ \frac{kGB}{3}\frac{1+\nu_u}{1-\nu_u}\left(\hat{\delta}_z + \int_0^t \hat{\delta}_z(t')K_2(t-t',k)dt'\right) - \frac{\mathcal{F}}{\mathcal{F}+1}\int_0^t \hat{p}_c(t')K_2(t-t',k)dt'. \tag{76}$$

3.6. Inversion of the fourier transform

The spectral boundary integral approach's pivotal step involves utilizing expressions, like those outlined in the preceding section, to ascertain relationships vital for simulations. These simulations could encompass areas like fracturing, frictional dynamics, or

solving flow problems. By expanding the fields associated with boundary conditions (e.g., slip, layer boundary pressure, or flux) in a Fourier series, this can be achieved with high efficiency. Although we will illustrate an example of this process, we will not transform every equation from Section 3.2 for brevity. Comprehensive explanations of this procedure can be found in prior works, such as those by Geubelle and Rice (1995), Lapusta et al. (2000), Heimisson et al. (2022).

Consider the 2D Fourier series of the slip in the x direction:

$$\delta_x(t, x, y) = \sum_{n=-N/2}^{N/2-1} \sum_{m=-M/2}^{M/2-1} D_x^{(n,m)}(t) e^{ik_x^n x + ik_y^m y}, \tag{77}$$

where $k_x^n = 2\pi n/L_x$ and $k_y^n = 2\pi n/L_y$ with L_x and L_x being the domain sizes in the x and y directions respectively and thus the domain is discretized in by $N \times M$ with an area of $L_x \times L_y$. The summation assumes N and M are even numbers. Similarly for δ_y we write

$$\delta_y(t, x, y) = \sum_{n=-N/2}^{N/2-1} \sum_{m=-M/2}^{M/2-1} D_y^{(n,m)}(t) e^{ik_x^n x + ik_y^m y}, \tag{78}$$

where $D_x^{(n,m)}(t)$ and $D_y^{(n,m)}(t)$ signify individual Fourier coefficients in each Fourier series for the two slip fields. Analogous expansions can be applied to other pertinent fields, like $p_c(t, x, y)$ or $J^+(t, x, y)$.

The equations in Section 3.2 provide a methodology to map the Fourier coefficients of known fields, which are associated with boundary conditions, to the Fourier coefficients of unknown fields, such as stress. For instance, Eq. (72) can be used to deduce the corresponding Fourier coefficient of $\sigma_{xz}(t)$.

$$\Sigma_{xz}^{n,m}(t) = -\frac{G}{2k^{(n,m)}} \left(\frac{(k_x^n)^2}{1 - \nu_u} \left(D_x^{(n,m)}(t') + \int_0^t D_x^{(n,m)}(t') K_1(t - t', k^{(n,m)}) dt' \right) + (k_y^m)^2 D_x^{(n,m)}(t') \right)$$
$$+ \frac{G k_x^n k_y^m}{2k^{(n,m)}} \left(D_y^{(n,m)}(t') - \frac{1}{1 - \nu_u} \left(D_y^{(n,m)}(t') + \int_0^t D_y^{(n,m)}(t') K_1(t - t', k^{(n,m)}) dt' \right) \right) \tag{79}$$

where then $k^{(n,m)} = \sqrt{(k_x^n)^2 + (k_y^m)^2} = \sqrt{(2\pi n/L_x)^2 + (2\pi m/L_y)^2}$ and L_x and L_y represent the size of the computational domain in the x and y dimensions.

In practical applications, Fourier coefficients $D_x^{(n,m)}$ and $D_y^{(n,m)}$ are determined at each time step using a two-dimensional fast Fourier transform (2D FFT). The above equation then operates on the $D_x^{(n,m)}$ and $D_y^{(n,m)}$ coefficients to compute the $\Sigma_{xz}^{n,m}$ coefficient. Subsequently, an inverse 2D FFT is employed to derive $\sigma_{xy}(t)$ from all $\Sigma_{xz}^{n,m}$ coefficients. For a comprehensive understanding of how this general methodology integrates into more complex frictional and fracture problem simulations, we direct readers to works by Geubelle and Rice (1995), Lapusta et al. (2000), Lapusta and Liu (2009), Heimisson et al. (2022).

This approach offers two primary advantages. Firstly, leveraging FFT and IFFT ensures operations scale as $\mathcal{O}(NM \log(NM))$. In contrast, addressing the problem through matrix multiplication, as seen in conventional boundary element methods, would lead to $\mathcal{O}(N^2 M^2)$ scaling. Secondly, the modal independence is evident as the $^{(n,m)}$ Fourier coefficient of σ_{xy}, denoted as $\Sigma_{xz}^{n,m}$, exclusively relies on other $^{(n,m)}$ Fourier coefficients. This means operations on each Fourier coefficient, like the convolution in Eq. (79), can be executed without referencing other Fourier coefficients. This facilitates parallel processing in a seamless manner.

4. In-plane pressure field of a penny-shaped crack

Frictional sliding on an interface within a poroelastic medium can lead to intriguing effects on frictional strength, effects that remain not fully understood. For mode II or in-plane sliding around a crack tip, compression and dilation lobes manifest on either side of the crack tip within the surrounding bulk. This anti-symmetry, while present in a simple linear elastic medium, does not alter the normal stress at the interface unless the materials on either side exhibit different compressibilities (e.g., Weertman, 1980). In an isotropic poroelastic medium, however, compression on one side of the rupture elevates the pore pressure, while dilation on the other side reduces it. This results in a pronounced gradient across the frictional interface. Such an effect has been postulated to potentially destabilize velocity-strengthening friction around a steady state, even with minor perturbations (Heimisson et al., 2019). This phenomenon mirrors the bimaterial effects observed by Rice et al. (2001) and the effective bimaterial effects due to the absence of geometrical reflection symmetry as noted by Aldam et al. (2016). The first term of Eq. (76) illustrates that in-plane slip across a layer leads to an increase in pore pressure on one side and a decrease on the other, exhibiting an anti-symmetric pattern. This is further depicted in Fig. 2.

The exact influence of pore pressure anti-symmetry on the frictional strength of the interface remains a topic of debate. Nonetheless, it has been proposed that the peak pore pressure across the interface might dictate the maximum frictional strength of the layer. If this hypothesis holds, the dynamics of such ruptures could be significantly impacted.

In Mode III or anti-plane sliding, there is no such effect, neither on a poroelastic material interface nor in bimaterial sliding. However, a interface rupture on a 2D plane in a 3D medium can be understood as the combination of mode II and III and perhaps mode I if there is a opening component or dilatation. To explore this further we solve Eq. (76).

Let us first delve into the relevant non-dimensional time scales. From the convolution kernels K_1 and K_2 we can infer two pertinent time scales:

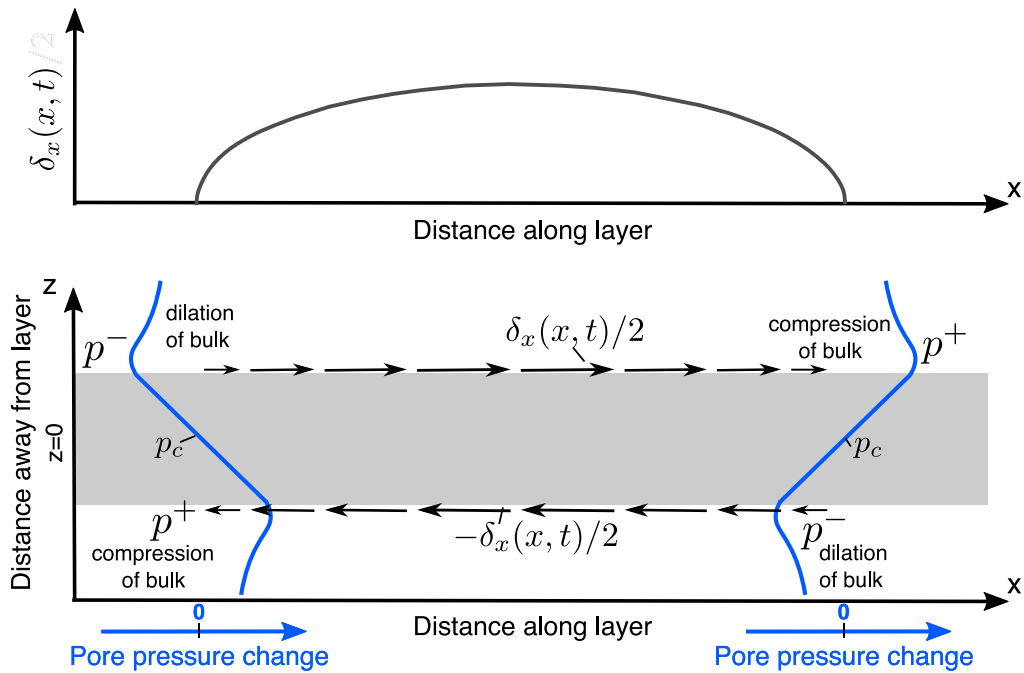$$t_b = \frac{1}{ck^2}, \tag{80}$$

Fig. 2. Schematic representation of the pressure induced by a typical mode II crack with an elliptical slip distribution across the layer. Given the assumed slip orientation, the pressure increases at one crack tip and decreases at the other. This is attributed to the compressional and dilatational lobes at the tip region, which induce pressure changes due to poroelastic coupling. On the opposite side of the layer, the pattern is inverted. This phenomenon is evident in the $\pm$ sign of the first term of Eq. (76) and the dependence on k_x in the same equation, indicating a directional pressure field dependency.

which denotes the diffusion time scale into the bulk. This scale is universally applicable across various boundary conditions, be it arbitrary flux, arbitrary pressure, or the bi-linear pressure. The second time scale is:

$$t_f = \frac{1}{\mathcal{F}^2 c k^2} = \frac{\kappa^2 \epsilon^2}{\kappa_c^2 c}, \tag{81}$$

which characterizes the rate at which pressure equilibrates across the layer under the bi-linear pressure model. The other boundary conditions do not explicitly define the flow properties of the layer. Nevertheless, it might be plausible to view this scale as approximately representative for most physical layers, especially when assuming they are thin relative to the x-y dimensions of the slip patch.

To better understand this, let us visualize the pressure field. We choose $k = 2\pi/R$, where R represents the radius of a penny-shaped crack with an elliptical opening (indicative of a constant stress drop crack). This gives $t_b = \frac{R^2}{4\pi^2 c}$. Notably, t_f remains independent of this length scale, provided the layer remains thin compared to the x-y dimensions of the slip patch.

Fig. 3 primarily visualizes the elastic response resulting from the crack slip, i.e., the undrained response. To replicate this figure using linear elasticity, one can utilize the relationship between volumetric stress and undrained pore pressure, given by $p_{un} = -B(\sigma_{kk})/3$.

A striking feature of the pressure distribution is the extensive pressure variation across a large portion of the crack. This occurs despite the mode III component of the fracture not inducing such a response. Research focusing on frictional ruptures under plane strain or mode II sliding has identified this pressure response as a significant factor influencing rupture dynamics (Rudnicki and Koutsibelas, 1991; Rudnicki and Rice, 2006; Jha and Juanes, 2014; Torberntsson et al., 2018; Heimisson et al., 2019, 2021). This observation implies that the effect might also be significant for a planar rupture in a 3D medium.

While the undrained response (Fig. 3) provides insights, it does not elucidate the time scales at which the coupled pore pressure and slip effects are relevant. To address this, we examine the pressure distribution in relation to the undrained response (Fig. 4). This comparison underscores the significance of the two time scales emerging from the bi-linear pressure distribution solutions: t_f and t_b. In scenarios where $t_f/t_b \ll 1$ (as seen in column **a** of Fig. 4), pore pressure dissipates via bulk diffusion, leading to pressure migration along the crack interface. Such migration might introduce intriguing effects, potentially allowing further destabilization of growing cracks through diffusion. However, this hypothesis requires validation in future studies. For $t_f/t_b = 1$ (column **b** in Fig. 4), pressure decreases more rapidly due to layer flux, driven by the pressure gradient depicted in Fig. 2. Yet, for $t_f/t_b = 10$ (column **c** in Fig. 4), pressure equilibrates swiftly across the layer, substantially diminishing the less-understood effect of slip-induced anti-symmetric pore pressure at the layer interface.

In conclusion, our simulations of the pressure distribution adjacent to a penny-shaped crack with an elliptical slip profile along the x-axis (as shown in Fig. 3**b**) using Eq. (76) reveal that a significant portion of the crack tip and interface undergoes notable pressure
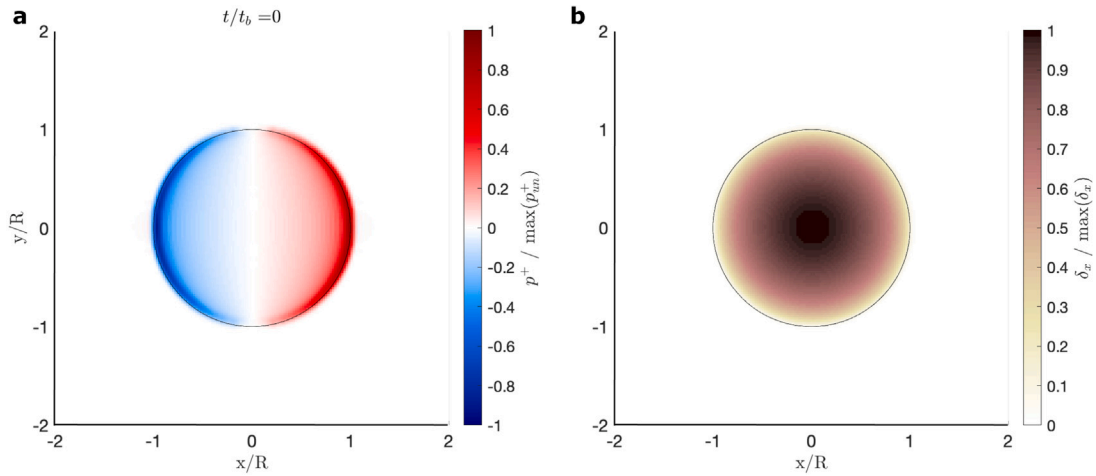
Fig. 3. The undrained pressure response (p^+) in **a** for a penny-shaped crack with the slip distribution δ_x shown in **b** (assuming δ_y and δ_z are 0). Both the pressure and slip distributions are normalized by their maximum values, and distances are normalized by the crack radius. The results reveal a pronounced anti-symmetric pressure response within the crack circle. Notably, the pressure response significantly affects most parts of the crack, excluding the center axis. This occurs even though the volumetric stress response of the surrounding medium is exclusive to mode II sliding.

changes. Moreover, when $t_f/t_b \lesssim 1$, the poroelastically induced pressure can migrate beyond the crack tip. We propose that the directional properties of the pressure distribution, combined with the migration of pressure changes along the crack plane, could profoundly influence frictional dynamics on interfaces where poroelasticity is a factor. This is particularly relevant for geotrials, biomaterials, soft materials, and gels.

5. Discussion

5.1. Potential inclusion of more complex physics

The primary objective of this work has been to present the spectral boundary integral (SBI) equations in a format applicable to carrying out simulations and to facilitate the understanding of various physically significant problems. In light of this, it is pertinent to address some of the limitations of the current approach and explore potential avenues for incorporating additional complexities, particularly focusing on inertial effects and non-planarity.

In considering inertial effects, it is crucial to address both the inertia of the layer and the bulk. The SBI equations for general flux and pressurization of the layer, while not making explicit assumptions about the layer's properties beyond its thinness, could potentially include inertial terms. However, the bulk physics in our current model assumes quasi-static deformation. Adapting these equations for a layer that accounts for inertial effects would necessitate modifications to the bulk physics as well.

Noda (2022) have successfully integrated elastodynamic spectral boundary integral convolution kernels at high slip rates, effectively treating the bulk as elastodynamic while maintaining an undrained poroelastic response. This approach has often proven effective (Heimisson and Rinaldi, 2022), yet it does not constitute a rigorous treatment of poroelastodynamics. In the bi-linear pressure distribution equations derived in our study, quasi-static Darcy's law is employed, explicitly excluding inertia effects. While it might be feasible to adapt Darcy's law to be compatible with poroelastodynamics (e.g., Cheng, 2016), this might not be advantageous without a rigorous treatment of a poroelastodynamic bulk.

However, treating the layer deformation as quasi-static may often be a reasonable approximation. Rice (2006) posited that if the layer is sufficiently thin, the stress variations over small distances are minimal, allowing for the inertia of the layer to be disregarded, even though it might be relevant for the bulk at larger slip scales. This assumption was further examined by Platt et al. (2014) in their thermo-poroelastic one-dimensional simulations. They proposed a critical slip velocity defined as:

$$V_c = \sqrt{\frac{\bar{\sigma}_a}{100\rho}}, \tag{82}$$

where ρ represents the density in a reference state of the gouge, and $\bar{\sigma}_a$ is the ambient effective normal stress. In many geophysical and geomechanical contexts, the ambient effective stress typically ranges from 10 to 100 MPa, with a density around 3000 kg/m^3. Consequently, the inertia of the layer becomes significant when the slip rate exceeds approximately 5 m/s, a velocity that is relatively high, but could occur in large seismic events. Such slip speed and larger has been observed in simulations (Dunham et al., 2011a,b). However, at these slip speeds, off-fault plasticity plays a significant role, which is a further complication that cannot easily be considered in a boundary integral formulation unless the plastic deformation of can be characterized as being within the thin layer.
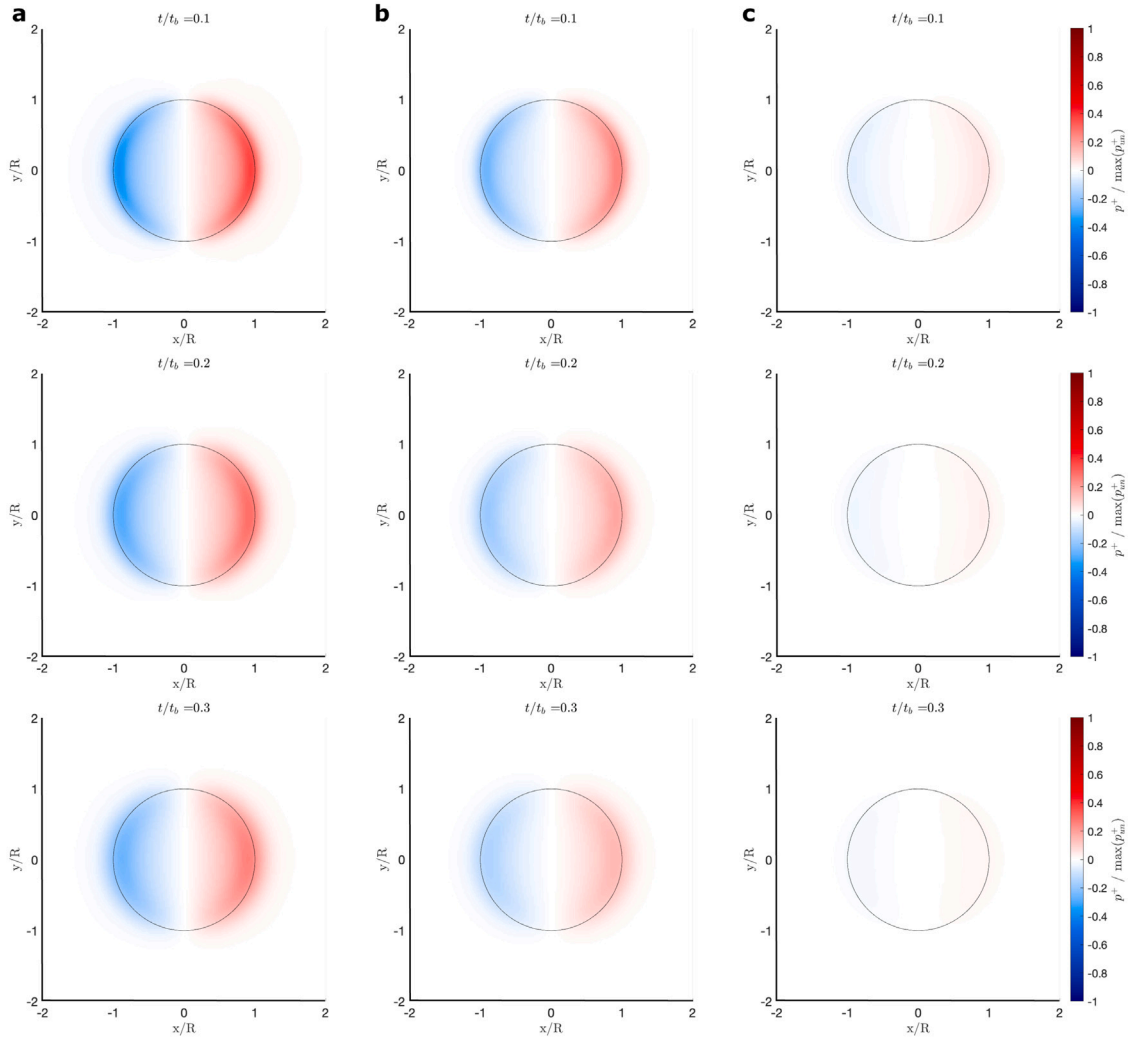
Fig. 4. Evolution of pore pressure (p^+) following an instantaneous slip on a penny-shaped crack (as depicted in Fig. 3). Column **a** assumes $t_f/t_b = 0$, **b** assumes $t_f/t_b = 1$, and **c** assumes $t_f/t_b = 10$. The top row represents time $t/t_b = 0.1$, the second row $t/t_b = 0.2$, and the third row $t/t_b = 0.3$. For low-permeability layers ($t_f/t_b \leq 1$), pressure dispersion occurs along the layer boundary. However, for high-permeability layers ($t_f/t_b = 10$), pressure equilibration happens swiftly through layer flux.

Another critical assumption in our analysis is the planarity of the layer. However, natural surfaces, including fractures and faults, are seldom perfectly planar. Geological faults, in particular, exhibit universal roughness, and it has been suggested that their topography may be statistically fractal in nature (Power et al., 1987). Consequently, there are likely scales or specific locations where the assumption of planarity does not hold true.

One approach to accommodate fault roughness is to conceptualize the rough surface as being encompassed within the thin layer. This method aligns with the strategies employed in hybrid methods that utilize purely elastic SBIM schemes (Hajarolasvadi and Elbanna, 2017; Ma et al., 2019; Albertini et al., 2021). While the half-space poroelastic SBI equations are not currently known analytically to the best of my knowledge, it is plausible that some of the terms would be consistent with those presented in this study.

The hybrid methods typically employ half-space SBI equations (Breitenfeld and Geubelle, 1998), they are thus less constrained by the need for a strict separation of scales. However, some degree of scale separation is still necessary to achieve notable improvements in computational efficiency. Recent advancements have demonstrated that mild non-planarity can be effectively approximated in elastodynamic SBI equations (Romanet and Ozawa, 2021). This suggests the potential for a similar approach to be applied in the context of poroelasticity. Such a development could significantly enhance the applicability of SBI methods in more complex, realistic geological scenarios where planarity cannot be assumed.

6. Conclusion

This study has advanced the application of the spectral boundary integral (SBI) method in terms of poroelastic media with potential applications of fluid-filled interfaces in natural and synthetic systems such as geological and biological layers. By deriving analytical SBI equations for 3D cracks and thin layers, we have provided a framework that can capture the complex interplay between poroelasticity, fracture mechanics, and fluid dynamics.

We present three core solutions, each tailored to specific boundary conditions in flow or pressure: arbitrary pressure, arbitrary flux, and a bi-linear pressure profile. The bi-linear pressure solution, in particular, serves as a versatile model for thin, leaky layers subject to pressurization. Further, it bridges parts the other two solutions under certain limiting cases of a non-dimensional parameters $\mathcal{F}$.

A significant insight from our work is the identification of in-plane pressure effects due to shear cracks in poroelastic solids. Contrary to the limited scope of mode II sliding in 2D, we demonstrate that in a 3D context, the pressurization impacts a substantial area of the crack face. This finding suggests a broader influence on the frictional strength of the interface than previously recognized.

Moreover, we have explored non-dimensional timescales that dictate the dynamics of pressure migration and its potential to extend beyond the crack tip. This suggests that poroelastic effects could propagate changes in frictional strength to regions away from the initial rupture, influencing the dynamics of crack growth and stability.

In conclusion, our analytical solutions offer a robust toolset for probing the mechanics of poroelastic interfaces. The potential to account for pressurization of the interface that can migrate and alter the frictional properties of a medium opens new avenues for understanding and predicting the behavior of fractures and faults in a variety of settings, from geological subsurfaces to engineered materials.

CRediT authorship contribution statement

Elías R. Heimisson: Writing – review & editing, Writing – original draft, Visualization, Validation, Supervision, Software, Resources, Project administration, Methodology, Investigation, Funding acquisition, Formal analysis, Conceptualization.

Declaration of competing interest

The authors declare that they have no known competing financial interests or personal relationships that could have appeared to influence the work reported in this paper.

Data availability

No data was used for the research described in the article.

Declaration of Generative AI and AI-assisted technologies in the writing process

During the preparation of this work the author used ChatGPT4 in order to proofread the manuscript (i.e. the text excluding equations) that was otherwise completely written. After using this tool, the author reviewed and edited the content as needed and takes full responsibility for the content of the publication.

Acknowledgments

References

Albertini, G., Elbanna, A.E., Kammer, D.S., 2021. A three-dimensional hybrid finite element — spectral boundary integral method for modeling earthquakes in complex unbounded domains. Internat. J. Numer. Methods Engrg. 122 (23), 6905–6923. http://dx.doi.org/10.1002/nme.6816.

Aldam, M., Bar-Sinai, Y., Svetlizky, I., Brener, E.A., Fineberg, J., Bouchbinder, E., 2016. Frictional sliding without geometrical reflection symmetry. Phys. Rev. X 6, 041023. http://dx.doi.org/10.1103/PhysRevX.6.041023.

Alghamdi, A., Hesse, M.A., Chen, J., Ghattas, O., 2020. Bayesian poroelastic aquifer characterization from InSAR surface deformation data. Part I: Maximum a posteriori estimate. Water Resour. Res. 56 (10), e2020WR027391. http://dx.doi.org/10.1029/2020WR027391.

Atkinson, C., Craster, R.V., 1991. Plane strain fracture in poroelastic media. Proc. R. Soc. Lond. Ser. A Math. Phys. Eng. Sci. 434 (1892), 605–633. http://dx.doi.org/10.1098/rspa.1991.0116, URL https://royalsocietypublishing.org/doi/abs/10.1098/rspa.1991.0116.

Barbot, S., 2021. A spectral boundary-integral method for quasi-dynamic ruptures of multiple parallel faults. Bull. Seismol. Soc. Am. 111 (3), 1614–1630. http://dx.doi.org/10.1785/0120210004, arXiv:https://pubs.geoscienceworld.org/ssa/bssa/article-pdf/111/3/1614/5315109/bssa-2021004.1.pdf.

Baumberger, T., Caroli, C., Ronsin, O., 2002. Self-healing slip pulses along a gel/glass interface. Phys. Rev. Lett. 88 (7), 075509.

Breitenfeld, M.S., Geubelle, P.H., 1998. Numerical analysis of dynamic debonding under 2D in-plane and 3D loading. Int. J. Fract. 93 (1), 13–38. http://dx.doi.org/10.1023/A:1007535703095.

Chang, K.W., Segall, P., 2016. Injection-induced seismicity on basement faults including poroelastic stressing. J. Geophys. Res. Solid Earth 121 (4), 2708–2726. http://dx.doi.org/10.1002/2015JB012561.

Cheng, A.H.-D., 2016. Poroelasticity, vol. 877, Springer.

Cheng, A.H.-D., Detournay, E., 1988. A direct boundary element method for plane strain poroelasticity. Int. J. Numer. Anal. Methods Geomech. 12 (5), 551–572. http://dx.doi.org/10.1002/nag.1610120508.

Cheng, A.H.-D., Detournay, E., 1998. On singular integral equations and fundamental solutions of poroelasticity. Int. J. Solids Struct. (ISSN: 0020-7683) 35 (34), 4521–4555. http://dx.doi.org/10.1016/S0020-7683(98)00082-1.

Cheng, A.H.-D., Liggett, J.A., 1984. Boundary integral equation method for linear porous-elasticity with applications to fracture propagation. Internat. J. Numer. Methods Engrg. 20 (2), 279–296. http://dx.doi.org/10.1002/nme.1620020207.

Detournay, E., Cheng, A.H.-D., 1995. Fundamentals of poroelasticity. In: Analysis and Design Methods. Elsevier, pp. 113–171.

Dunham, E.M., Belanger, D., Cong, L., Kozdon, J.E., 2011a. Earthquake ruptures with strongly rate-weakening friction and off-fault plasticity, part-1: Planar faults. Bull. Seismol. Soc. Am. (ISSN: 0037-1106) 101 (5), 2296–2307. http://dx.doi.org/10.1785/0120100075.

Dunham, E.M., Belanger, D., Cong, L., Kozdon, J.E., 2011b. Earthquake ruptures with strongly rate-weakening friction and off-fault plasticity, part-2: Nonplanar faults. Bull. Seismol. Soc. Am. (ISSN: 0037-1106) 101 (5), 2308–2322. http://dx.doi.org/10.1785/0120100076.

Galeano, J., Espanol, P., Rubio, M., 2000. Experimental and theoretical results of stress relaxations in a model of earthquake dynamics. Europhys. Lett. 49 (4), 410.

Geubelle, P.H., Breitenfeld, M.S., 1997. Numerical analysis of dynamic debonding under anti-plane shear loading. Int. J. Fract. 85 (3), 265–282. http://dx.doi.org/10.1023/A:1007498300031.

Geubelle, P.H., Rice, J.R., 1995. A spectral method for three-dimensional elastodynamic fracture problems. J. Mech. Phys. Solids (ISSN: 0022-5096) 43 (11), 1791–1824. http://dx.doi.org/10.1016/0022-5096(95)00043-I.

Hajarolasvadi, S., Elbanna, A.E., 2017. A new hybrid numerical scheme for modelling elastodynamics in unbounded media with near-source heterogeneities. Geophys. J. Int. (ISSN: 0956-540X) 211 (2), 851–864. http://dx.doi.org/10.1093/gji/ggx337.

Heimisson, E.R., Dunham, E.M., Almquist, M., 2019. Poroelastic effects destabilize mildly rate-strengthening friction to generate stable slow slip pulses. J. Mech. Phys. Solids (ISSN: 0022-5096) 130, 262–279. http://dx.doi.org/10.1016/j.jmps.2019.06.007.

Heimisson, E.R., Liu, S., Lapusta, N., Rudnicki, J., 2022. A spectral boundary-integral method for faults and fractures in a poroelastic solid: Simulations of a rate-and-state fault with dilatancy, compaction, and fluid injection. J. Geophys. Res. Solid Earth 127 (9), e2022JB024185. http://dx.doi.org/10.1029/2022JB024185.

Heimisson, E.R., Rinaldi, A.P., 2022. Spectral boundary integral method for simulating static and dynamic fields from a fault rupture in a poroelastodynamic solid. Geomech. Geophys. Geo-Energy Geo-Res. 8 (2), 1–20. http://dx.doi.org/10.1007/s40948-022-00368-4.

Heimisson, E.R., Rudnicki, J., Lapusta, N., 2021. Dilatancy and compaction of a rate-and-state fault in a poroelastic medium: Linearized stability analysis. J. Geophys. Res. Solid Earth 126 (8), e2021JB022071. http://dx.doi.org/10.1029/2021JB022071.

Jha, B., Juanes, R., 2014. Coupled multiphase flow and poromechanics: A computational model of pore pressure effects on fault slip and earthquake triggering. Water Resour. Res. 50 (5), 3776–3808. http://dx.doi.org/10.1002/2013WR015175.

Jónsson, S., Segall, P., Pedersen, R., Björnsson, G., 2003. Post-earthquake ground movements correlated to pore-pressure transients. Nature 424 (6945), 179–183. http://dx.doi.org/10.1038/nature01776.

Lapusta, N., Liu, Y., 2009. Three-dimensional boundary integral modeling of spontaneous earthquake sequences and aseismic slip. J. Geophys. Res. Solid Earth 114 (B9), http://dx.doi.org/10.1029/2008JB005934.

Lapusta, N., Rice, J.R., Ben-Zion, Y., Zheng, G., 2000. Elastodynamic analysis for slow tectonic loading with spontaneous rupture episodes on faults with rate-and state-dependent friction. J. Geophys. Res. Solid Earth 105 (B10), 23765–23789. http://dx.doi.org/10.1029/2000JB900250.

Lubis, A.M., Hashima, A., Sato, T., 2012. Analysis of afterslip distribution following the 2007 September 12 southern Sumatra earthquake using poroelastic and viscoelastic media. Geophys. J. Int. (ISSN: 0956-540X) 192 (1), 18–37. http://dx.doi.org/10.1093/gji/ggs020.

Ma, X., Hajarolasvadi, S., Albertini, G., Kammer, D.S., Elbanna, A.E., 2019. A hybrid finite element-spectral boundary integral approach: Applications to dynamic rupture modeling in unbounded domains. Int. J. Numer. Anal. Methods Geomech. 43 (1), 317–338. http://dx.doi.org/10.1002/nag.2865.

McNamee, J., Gibson, R.E., 1960. Plane strain and axially symmetric problems of the consolidation of a semi-infinite clay stratum. Q. J. Mech. Appl. Math. 13 (2), 210–227.

Noda, H., 2022. Dynamic earthquake sequence simulation with an SBIEM accounting for interseismic poroelastic rebound. Earth Planets Space 74 (1), 1–15.

Norbeck, J.H., McClure, M.W., Horne, R.N., 2018. Field observations at the Fenton Hill enhanced geothermal system test site support mixed-mechanism stimulation. Geothermics (ISSN: 0375-6505) 74, 135–149. http://dx.doi.org/10.1016/j.geothermics.2018.03.003.

Perrin, G., Rice, J.R., 1994. Disordering of a dynamic planar crack front in a model elastic medium of randomly variable toughness. J. Mech. Phys. Solids (ISSN: 0022-5096) 42 (6), 1047–1064. http://dx.doi.org/10.1016/0022-5096(94)90083-3.

Platt, J.D., Rudnicki, J.W., Rice, J.R., 2014. Stability and localization of rapid shear in fluid-saturated fault gouge: 2. Localized zone width and strength evolution. J. Geophys. Res. Solid Earth 119 (5), 4334–4359. http://dx.doi.org/10.1002/2013JB010711.

Power, W.L., Tullis, T.E., Brown, S.R., Boitnott, G.N., Scholz, C.H., 1987. Roughness of natural fault surfaces. Geophys. Res. Lett. 14 (1), 29–32. http://dx.doi.org/10.1029/GL014i001p00029.

Quin, H., Das, S.X., 1989. A hybrid boundary integral equation method for the computation of source time functions for 3-D rupture propagation. Geophys. J. Int. 96 (1), 163–177. http://dx.doi.org/10.1111/j.1365-246X.1989.tb05258.x.

Rice, J.R., 1993. Spatio-temporal complexity of slip on a fault. J. Geophys. Res. Solid Earth 98 (B6), 9885–9907. http://dx.doi.org/10.1029/93JB00191.

Rice, J.R., 2006. Heating and weakening of faults during earthquake slip. J. Geophys. Res. Solid Earth 111 (B5), http://dx.doi.org/10.1029/2005JB004006.

Rice, J.R., Cleary, M.P., 1976. Some basic stress diffusion solutions for fluid-saturated elastic porous media with compressible constituents. Rev. Geophys. 14 (2), 227–241. http://dx.doi.org/10.1029/RG014i002p00227.

Rice, J.R., Lapusta, N., Ranjith, K., 2001. Rate and state dependent friction and the stability of sliding between elastically deformable solids. J. Mech. Phys. Solids 49 (9), 1865–1898.

Rice, J.R., Rudnicki, J.W., Platt, J.D., 2014. Stability and localization of rapid shear in fluid-saturated fault gouge: 1. Linearized stability analysis. J. Geophys. Res. Solid Earth 119 (5), 4311–4333. http://dx.doi.org/10.1002/2013JB010710.

Rinaldi, A.P., Improta, L., Hainzl, S., Catalli, F., Urpi, L., Wiemer, S., 2020. Combined approach of poroelastic and earthquake nucleation applied to the reservoir-induced seismic activity in the Val d'Agri area, Italy. J. Rock Mech. Geotechn. Eng. (ISSN: 1674-7755) 12 (4), 802–810. http://dx.doi.org/10.1016/j.jrmge.2020.04.003.

Romanet, P., Ozawa, S., 2021. Fully dynamic earthquake cycle simulations on a non-planar fault using the spectral boundary integral element method. arXiv:2107.03550.

Ronsin, O., Baumberger, T., Hui, C., 2011. Nucleation and propagation of quasi-static interfacial slip pulses. J. Adhesion 87 (5), 504–529.

Rudnicki, J.W., Koutsibelas, D.A., 1991. Steady propagation of plane strain shear cracks on an impermeable plane in an elastic diffusive solid. Int. J. Solids Struct. 27 (2), 205–225.

Rudnicki, J.W., Rice, J.R., 2006. Effective normal stress alteration due to pore pressure changes induced by dynamic slip propagation on a plane between dissimilar materials. J. Geophys. Res.: Solid Earth 111 (B10), http://dx.doi.org/10.1029/2006JB004396.

Schiffman, R.L., Fungaroli, A., 1965. Consolidation due to tangential loads. In: Soil Mech & Fdn Eng Conf Proc/Canada/. pp. 188–192.

Segall, P., Lu, S., 2015. Injection-induced seismicity: Poroelastic and earthquake nucleation effects. J. Geophys. Res.: Solid Earth 120 (7), 5082–5103.

Smith, J.D., Heimisson, E.R., Bourne, S.J., Avouac, J.-P., 2022. Stress-based forecasting of induced seismicity with instantaneous earthquake failure functions: Applications to the Groningen gas reservoir. Earth Planet. Sci. Lett. (ISSN: 0012-821X) 594, 117697. http://dx.doi.org/10.1016/j.epsl.2022.117697.

Song, Y., Rudnicki, J.W., 2017. Plane-strain shear dislocation on a leaky plane in a poroelastic solid. J. Appl. Mech. 84 (2), 021008.

Torberntsson, K., Stiernström, V., Mattsson, K., Dunham, E.M., 2018. A finite difference method for earthquake sequences in poroelastic solids. Computat. Geosci. (ISSN: 1573-1499) 22 (5), 1351–1370. http://dx.doi.org/10.1007/s10596-018-9757-1.

Verruijt, A., 1971. Displacement functions in the theory of consolidation or in thermoelasticity. Z. Angew. Math. Phys. 22 (5), 891–898.

Weertman, J., 1980. Unstable slippage across a fault that separates elastic media of different elastic constants. J. Geophys. Res.: Solid Earth 85 (B3), 1455–1461.

Yoon, J., Cai, S., Suo, Z., Hayward, R.C., 2010. Poroelastic swelling kinetics of thin hydrogel layers: comparison of theory and experiment. Soft Matter 6 (23), 6004–6012.